Astronomy & Astrophysics manuscript no. output
July 23, 2021

Detection of period spacing patterns due to gravity modes of rotating dwarfs in the TESS Southern Continuous Viewing Zone

S. Garcia[1], T. Van Reeth[1], J. De Ridder[1], A. Tkachenko[1], L. IJspeert[1], and C. Aerts[1,2,3]

[1] Instituut voor Sterrenkunde (IvS), KU Leuven, Celestijnenlaan 200D, B-3001 Leuven, Belgium
e-mail: stefanorenzo.garciacastaneda@kuleuven.be
[2] Department of Astrophysics, IMAPP, Radboud University Nijmegen, PO Box 9010, 6500 GL, Nijmegen, The Netherlands
[3] Max Planck Institute for Astronomy, Koenigstuhl 17, 69117, Heidelberg, Germany

Received MM DD, 2021; accepted MM DD, 2021

ABSTRACT

Context. The theory of stellar evolution presents shortcomings when confronted with asteroseismic probes of interior physical properties. The differences between observations and theory are often large because stellar models have mainly been calibrated from observables connected to the surface of stars. Period spacing patterns due to gravity modes are a particularly powerful asteroseismic tool to probe the near-core rotation and mixing of chemical elements in stars with convective cores.
Aims. We aim to compose a catalogue of intermediate-mass stars in the Transiting Exoplanet Survey Satellite (TESS) Southern Continuous Viewing Zone (S-CVZ) revealing period spacing patterns caused by gravity modes. This TESS S-CVZ catalogue of dwarfs will allow for their future asteroseismic modelling.
Methods. TESS Full-Frame-Images were inspected to selected stars of intermediate- and high mass using colour-magnitude criteria. Light curves were extracted from custom masks per star, adopting stringent constraints on the aperture masks and contamination. The extracted light curves were subjected to iterative prewhitening in order to detect gravity modes. We developed a method relying on the assumption that period spacings are an approximately linear function of the mode periods to build a template pattern. This template was used to extract the patterns and their uncertainties, relying on a bootstrap approach.
Results. Our TESS catalogue of high-quality period spacing patterns is the first of its kind and contains 174 gravity-mode patterns in 128 γ Dor stars and 2 slowly pulsating B stars. Half of these patterns constitute of 7 or more measured mode periods and the longest pattern contains 18 modes. We provide the community with a convenient software tool to search for period spacing patterns from raw TESS images and to process the extracted light curves.
Conclusions. Our catalogue offers a fruitful starting point for future gravity-mode asteroseismology of rotating dwarfs with convective cores in the Southern Hemisphere.

Key words. Asteroseismology – Waves – Stars: Rotation – Stars: Interiors – Stars: oscillations (including pulsations) – Stars: catalogue

1. Introduction

The theory of stellar structure and evolution is well established and capable to describe the different stages of a star throughout its life in general terms (e.g. Kippenhahn et al. 2012). However, the theory is mostly calibrated to surface properties of stars, such as its surface gravity, surface chemical composition, surface rotation and effective temperature. Today, advances in asteroseismology and the advent of high-precision space photometry from telescopes such as CoRoT (Auvergne et al. 2009), *Kepler* (Koch et al. 2010) and TESS (Ricker et al. 2015) allow us to probe stellar interiors with a precision that cannot be reached from extrapolating surface quantities (e.g Hekker & Christensen-Dalsgaard 2017; García & Ballot 2019; Aerts 2021, for recent reviews). Asteroseismic modelling based on space photometry have revealed large discrepancies between observations and the theory of stellar structure and evolution, e.g. for the transport of angular momentum (e.g., Aerts et al. 2019).

Gravity modes (hereafter g modes) are stellar oscillations that have buoyancy as their dominant restoring force and have optimal probing power in the near-core regions (e.g., Aerts et al. 2018). They are detected in main-sequence stars with a convective core and a radiative envelope known as γ Doradus (γ Dor) stars (Kaye et al. 1999) and Slowly Pulsating B-type (SPB) stars (Waelkens 1991), which have masses from 1.3 to 1.9 $M_\odot$ and 3 to 9 $M_\odot$, respectively (e.g., Aerts et al. 2010, Chapter 2, for more properties). To detect and accurately measure the frequencies of their individual g modes, which have periodicities of the order of days, high-precision long-term uninterrupted observations are needed. These requirements are met for time-series photometry from space missions such as *Kepler* and TESS, which allows us to detect g-mode period-spacing patterns. The first such detection in a dwarf was made for the SPB star HD 50230 from CoRoT space photometry by Degroote et al. (2010). The 5-month CoRoT light curve was sufficient to detect a period spacing pattern of 8 dipole g modes thanks to this star's very slow rotation, justifying as well asteroseismic modelling from ignoring the Coriolis acceleration in the pulsation computations (Wu & Li 2019).

Gravity-mode period spacing patterns, i.e., the difference in periods of g modes with identical spherical degree ℓ and azimuthal order m while having consecutive radial order n, are a powerful asteroseismic tool (Aerts et al. 2010, for a detailed theoretical derivation). This tool allows us to probe the near-core regions of main-sequence stars having a convective core and

a radiative envelope. As shown by Shibahashi (1979) and Tassoul (1980), g-mode periods $P_{n\ell}$ are equidistant for a spherical chemically homogeneous non-rotating star when considering the asymptotic regime, i.e. with $2\pi/P_{n\ell} \ll N$ with N the buoyancy frequency:

$$P_{nl} = \frac{\Pi_0}{\sqrt{\ell(\ell+1)}}\,(n+\epsilon_g), \tag{1}$$

with

$$\Pi_0 = \frac{2\pi^2}{\int_{r_1}^{r_2} N(r)\,r^{-1}\,\mathrm{d}r} \tag{2}$$

where ϵ_g is a phase term which depends on the boundaries r_1 and r_2 of the g-mode propagation cavity. Gradients in the stellar chemical composition profile cause mode trapping, which introduces wave-like behaviour and periodic dips also known as buoyancy glitches in the period-spacing patterns. As shown by Miglio et al. (2008), the amplitude and location of these modulations in the pattern depend on the steepness and the location of the chemical gradients inside the star.

For a rotating star, the Coriolis acceleration and the difference between the corotating and the observer's inertial reference frames shift the g-mode frequencies quite drastically. As a result, the observed period spacings reveal a decreasing trend for prograde ($m > 0$) and zonal ($m = 0$) modes when plotted as a function of increasing mode period as observed in an inertial frame of reference. For retrograde modes ($m < 0$), on the other hand, an overall increase in the observed spacings of modes with increasing pulsation period occurs (e.g., Bouabid et al. 2013; Van Reeth et al. 2015a,b; Ouazzani et al. 2017). Schmid & Aerts (2016) investigated the limit of the rotation frequency at which the Coriolis acceleration can still be treated perturbatively and found this approximation to already break down for rotation frequencies above roughly $\sim 0.1\,\mathrm{d}^{-1}$, which is the case for almost all intermediate-mass dwarfs (cf. Aerts et al. 2017).

A strong magnetic field in the stellar interior further requires the Lorentz force to be included in the pulsation computations. This modifies the morphology of the observed period spacing pattern by introducing a saw-tooth modulation of the period-spacing values as the consecutive pulsation periods increase (Van Beeck et al. 2020). Moreover, coupling between inertial modes in the rotating core and g modes in the envelope occurs and may cause dips superposed to buoyancy glitches at particular mode periods in the spacing diagram (Ouazzani et al. 2020; Saio et al. 2021; Lee 2021). This implies that interpretations of buoyancy glitches from mathematical analytical descriptions ignoring the Coriolis acceleration (e.g., Cunha et al. 2019) can only be applied to slowly-rotating non-magnetic stars. The majority of g-mode pulsators requires the modelling and interpretation of the observed period spacing patterns to be done numerically, based on inclusion of the Coriolis (and perhaps Lorentz) force when solving the pulsation equations (cf. Townsend & Teitler 2013; Townsend et al. 2018).

After the initial discovery by Degroote et al. (2010), it took another five years before period spacing patterns were detected from 4-year *Kepler* light curves in several hundreds of γ Dor stars (e.g., Van Reeth et al. 2015b; Li et al. 2019, 2020) and several dozens of SPB stars (e.g. Pápics et al. 2017; Pedersen et al. 2021; Szewczuk et al. 2021). These patterns have been used to measure the near-core rotation rates of all these stars (e.g., Van Reeth et al. 2016; Christophe et al. 2018; Van Reeth et al. 2018; Li et al. 2019, 2020; Takata et al. 2020; Pedersen et al. 2021) and place constraints on the chemical transport processes that take place in the deep stellar interior (e.g. Mombarg et al. 2019, 2020; Pedersen et al. 2021). From the point of view of improving stellar evolution theory, dwarfs are the most interesting targets as they still have their evolved stages ahead of them and uncertainties in the transport processes are cumulative over time. Moreover, g modes are are potentially excited along the main sequence in various instability regions for stars born with a convective core covering a large mass range (Aerts et al. 2010, Chapter 3). This is why we focus our work on dwarfs covering spectral types from F to O.

To date, the photometric observations obtained with the nominal *Kepler* mission cover the longest time base and are more precise than the observations from any other high-cadence space-photometry mission. Hence, most breakthroughs in g-mode asteroseismology of dwarfs were achieved thanks to *Kepler* observations so far. Here, we exploit the asteroseismic potential of the ongoing TESS space mission and compare it to the one of *Kepler*. The TESS extended mission is gradually providing data of progressively high-frequency resolution and has opened the door to analyse numerous stars located in regions of the sky other than the *Kepler* field of view. In this work we present results based on the first full year of uninterrupted TESS monitoring, to evaluate its capacity for g-mode asteroseismology of rotating dwarfs. Future work will involve the addition of data from the extended TESS mission to the stars in our current catalogue, to increase their capacity of asteroseismic modelling.

We aim at identifying new γ Dor or SPB stars that have been observed by TESS in the Southern Continuous Viewing Zone (S-CVZ) to build the first catalogue of high-quality g-mode period spacing patterns for such pulsators. The S-CVZ was observed uninterruptedly during the first year of the nominal TESS mission, with a 24° square field-of-view centred at the Southern ecliptic pole rotating about every 27 d. This long observation leads to light curves with a nominal frequency resolution of about $0.003\mathrm{d}^{-1}$.

The paper is organised as follows. In Section 2 we describe our criteria for selecting O/B- and A/F-type stars in the TESS S-CVZ. In Section 3 we describe our method used to extract light curves from the TESS full-frame images (FFI), including our data analysis treatments to detrend and optimise the extracted light curves to search for g modes. In Section 4 we discuss the frequency extraction from the light curves and our posterior analysis. Section 5 describes our method to find the period spacing patterns. Finally, we discuss our final catalogue of g-mode pulsators with period spacing patterns in Section 6.

2. Data set

To select our sample of stars we started from the TESS Input Catalogue (TIC) version 8 (Stassun et al. 2019) and reduced it to the TESS S-CVZ by imposing an ecliptic latitude $\beta \leq -72°$. To exclude extended objects and keep only point-like sources, we used the TIC's flag `Objtype=star`. Stars likely to be white dwarfs or giants were identified with the TIC's flag `wdflag=1` and `lumclass=GIANT`, respectively, and excluded from the sample. The first flag represents a cut in absolute *Gaia* magnitude and *Gaia* colour ($G_{BP} - G_{RP}$) while the second flag represents a cut in radius (calculated from *Gaia* parallaxes) and $T_{\rm eff}$. The reader is refered to Stassun et al. (2019) for a description of the TIC flags.

To narrow down our sample of stars to candidates of spectral type F and hotter, i.e., the most likely g-mode pulsators, we used 139 TESS O/B-type stars selected manually by Pedersen et al. (2019) and 616 *Kepler* A/F-type γ Dor pulsators taken from

Tkachenko et al. (2013); Li et al. (2020). We placed those stars in a colour-magnitude diagram (CMD) and used them to define two pairs of colour-magnitude cuts that enclose 95% of these bona fide O/B- and A/F-type stars. By applying these pairs of cuts to our TESS sample, we extract all the O/B- and A/F-type candidate pulsators of interest. We calculated their absolute magnitudes as

$$M = m - 5\log(d) + 5, \quad (3)$$

where m is the apparent magnitude. To obtain the distance d, we used the Bayesian distance estimate from Bailer-Jones et al. (2018) reported in the TIC. To ensure reliable distances, we used stars with a positive *Gaia* parallax of relative error less than 25% that passed both astrometric and photometric criteria given by Eqs. (1) and (2) in Arenou et al. (2018) (i.e., TIC flag `gaiaqflag=1`). To minimize the effect of extinction, we used the 2MASS infrared bands J, H and K and adopted the cuts listed in Table 1. Figure 1 shows these cuts in K and $J-K$ as straight lines and our sample in the background. A/F-type candidates correspond to stars in the top-left quadrant delineated by the red straight lines minus the O/B-type candidates that correspond to stars in the top-left quadrant delineated by the cyan straight lines. The final candidates are obtained after an analogous additional selection in a CMD based on H and $J-H$. Table 1 and Figure 1 do not consider corrections for extinction. The potential contamination by cooler stars that are not expected to pulsate in g modes will be treated in Section 4, based on the frequency analysis results.

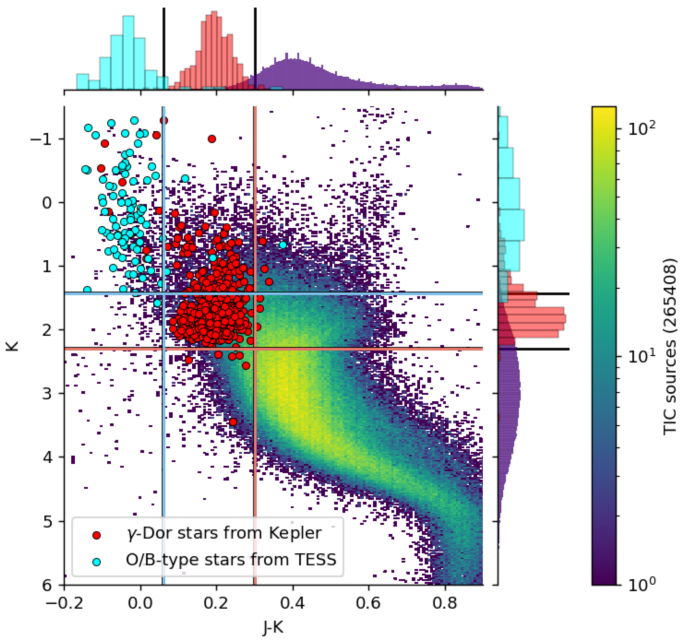

Fig. 1. CMD showing the pairs of cuts of absolute magnitude and colour defining candidate g-mode pulsators of spectral type O/B (cyan straight lines) and A/F (red straight lines) in K and $J-K$. The cyan and red circles are bona fide O/B- and A/F-type stars, respectively, while the retained dwarfs from the TIC in the S-CVZ are plotted in the background. The side histograms show the distribution of stars; the pairs of cuts enclose 95% of the respective bona fide stars.

Finally, to favour a high signal-to-noise ratio (SNR) and non-contaminated flux in the light curves, we limited our sample further to stars with apparent TESS magnitude brighter than 15 (uncorrected for extinction) and situated at least 2 arcsec apart from other stars in the TIC. Our selected sample consists of 345 O/B-type candidates and 9369 A/F-type candidates in the TESS S-CVZ.

Table 1. Pairs of cuts of absolute magnitude and colour in the 2MASS system (uncorrected for extinction) used to define O/B- and A/F-type candidates. The pairs of K and $J-K$ are displayed in Figure 1.

Spectral type candidate	K	$J-K$	H	$J-H$
O/B	1.429	0.06	1.55	0.045
A/F	2.300	0.30	2.35	0.240

3. Our TESS data reduction pipeline

We searched sectors 1 to 13 of TESS for long-cadence (i.e. 27.4 minutes) full-frame images (FFI) available in the Mikulski Archive for Space Telescopes (MAST) and used the `TESScut` API (Brasseur et al. 2019) to download, for every stars in our sample, a 20×20 pixel image with the target star at the centre. These images are known as Target Pixel Files (TPF) and contain the flux information for all available time stamps. The 20×20 pixel size was chosen such that the TPF contains both the flux of the target star and the flux of the representative background around it; a typical example is shown in Fig. 2 where the middle panel shows a background mask 11 times larger than the aperture mask. Light curves were extracted from the TPFs using simple aperture photometry (SAP) while the background and systematic effects were corrected using a principal component analysis (PCA).

3.1. Aperture and background masks

To define the aperture mask of a star, we used the median frame of all the TPFs (left panel in Fig. 2) and selected all pixels with a flux count larger than the median flux plus n-times the standard deviation. Those pixels are our first estimate of the aperture mask. The standard deviation was robustly estimated as 1.4826 times the median absolute deviation (Ruppert 2011). To reduce the contamination from nearby stars falling into the aperture mask, we used the increasing values of $n = 5.0, 7.5, 10, 15, 20, 30$, and 40 for the threshold in standard deviation to shrink the aperture mask until the target star was the only bright star contained within it. Neighbouring stars down to 4 TESS magnitudes fainter than the target star (white circles in Fig. 2) were excluded, ensuring that the flux of individual fainter stars contributes no more than $\sim 0.25\%$ of the total flux within the aperture mask. For cases where the resulting aperture mask consists of disjoint sets of pixels, only the set containing the target star is kept. Finally, to help prevent flux from neighbouring stars to leak into the aperture mask, pixels showing an increase in flux in the direction away from the target star are removed from the mask and used as its edge. The background mask was defined in the same way as the first estimate of the aperture mask but selecting the pixels below a threshold with $n = 3$, thus ensuring a minimum two-standard-deviation flux gap between the aperture mask and the background mask. A typical example of both final apertures is shown in the middle panel of Fig. 2.

To estimate the level of contamination in the aperture mask due to the flux of neighbouring stars, we calculate the ratio of this flux to that of the target star. To obtain such fluxes, all stars down to 4 TESS magnitudes fainter than the target were modelled as 2-D Gaussian functions and fitted to the median image of the

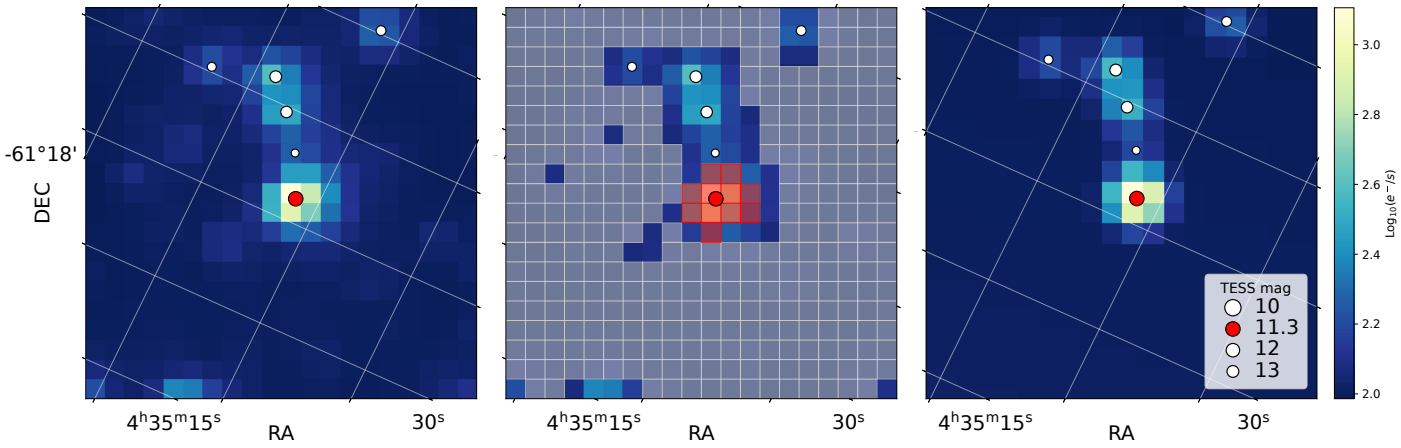

Fig. 2. Square 20-by-20 pixels around TIC 38845463, sector 1. The colour bar is common to the three panels and shows a logarithmic scale of the flux in electrons per second. Red circles represent the target star while white circles indicate TIC neighbouring stars up to 4 TESS magnitudes fainter with respect to the target star. The symbol sizes are inversely proportional to the TESS magnitude. *Left* - Median image based on all target pixels files of all available time stamps. *Middle* - panel with the final aperture mask (red shade) and background mask (grey shade) overplotted. The aperture mask results from the threshold parameter $n = 20$ (see text for explanation). *Right* - Best fit based on the left panel used to estimate the level of contamination in the aperture mask due to flux from neighbouring stars. The image was modelled as six 2-D Gaussian functions plus a 2-D plane. See Section 3.1 for further details.

TPF along with a 2-D plane to account for the background flux. The Gaussian functions were centred at the location of each star, had all the same standard deviation, and their relative amplitudes kept the same relation as their fluxes (converted from their TESS magnitudes using the TASOC Photometry pipeline[1]). The right panel in Fig. 2 shows an example of this fit.

We rejected the aperture mask (together with the TPF) when the final mask contained multiple stars. To avoid both corrupted and bleeding pixels, we also rejected masks that had pixels with null counts or that were too elongated (i.e., with less than 4 rows or columns, while the other is at least 14-pixels long). To average out the stochastic noise of individual pixels, we only kept aperture masks with at least 9 pixels, as shown in the left panel of Fig. 3. After careful assessment, our sample consisted of 2162 stars with a flux contamination due to neighbouring stars smaller than 5%, as shown in the right panel in Fig. 3. The middle panel in Fig. 3 shows that our light curve extraction is consistent with previous data pipelines for which the extraction is considered to be trustworthy only for stars brighter than TESS magnitude 13.5 (e.g Handberg et al. 2019; Huang 2020; Caldwell et al. 2020).

Because of our stringent constraints on the aperture mask, not all TESS sectors yielded a satisfactory mask for a given star. We therefore only kept stars with aperture masks found in at least 11 of the 13 TESS sectors, as shown by the dashed line in Fig. 4. After this cut, our sample consists of 1967 stars. Figure 4 also shows a higher level of contamination when the aperture mask is found in fewer numbers of TESS sectors, indicating that stars in a crowded field are more prone to fail the requirements of the aperture mask.

3.2. Light curve extraction and correction

To remove part of the systematic flux variability in the extracted light curves, we used the TPF data quality flags[2] (Twicken et al. 2020) and removed the data from the time stamps affected by loss of fine pointing[3], thermal transients[4], Earth pointing, and other specific effects[5] (e.g., coronal mass ejections). We then extracted the light curves using SAP with the aperture masks we constructed as described in Section 3.1. An example is shown in Fig. 5 where the gaps in the data correspond to the removed time stamps. We noted that the use of the quality flags according to the TESS release notes did not cover all systemics present in the light curves and proceeded to manually remove time intervals (common to all stars) which still were significantly affected by systematic effects (e.g. telescope jittering, thermal transients and loss of fine pointing). Such time intervals are present in sectors 1 to 8, as listed in Table A.1 and shown in red in Fig. 5.

To remove the remaining systematic variability and background flux (e.g., the gradual increase of flux in sector 2 due to scattered light or the rapid decrease of flux at the beginning of sector 8 as illustrated in Fig. 5), we used the Python package Lightkurve (Lightkurve Collaboration et al. 2018). We performed a principle component analysis (PCA) on the flux in the background mask defined in Section 3.1 and then used the result to perform a linear regression against the raw extracted light curve. We first extracted a SAP light curve from each pixel of the background mask. Subsequently, we used PCA on those light curves to obtain their main shared features, i.e. the trend of the background flux. Because each TESS sector is subjected to different systematic effects, no universal number of principle components (PCs) can be used. We opted for calculating the 7 dominant PCs for all TPF. For the final regression we used only those PCs that showed a well defined trend while discarding the ones that picked up mostly white noise, as shown in Fig. 6. To detect those PCs representing white noise, we partitioned them into chunks of 16 hours and estimated the PC's variance as the mean of the chunk's variance. If the PC's variance was larger than 10^{-4}, then that PC and the ones with lower eigenvalues were discarded. We used the same threshold value for all TPFs since PCs are normalised. Next we added a constant column to the regressor matrix to also account for a fixed background level. We then created the regressor matrix $\mathbf{X}$ using the PCs as its columns

[1] `https://github.com/tasoc`

[2] Descriptions about TESS quality flags can be found in the section "Data Product Overview" in `https://outerspace.stsci.edu/display/TESS`.

[3] Flagged as attitude tweak, coarse pointing and desaturation event.

[4] Flagged as safe mode.

[5] Flagged as manual exclude.

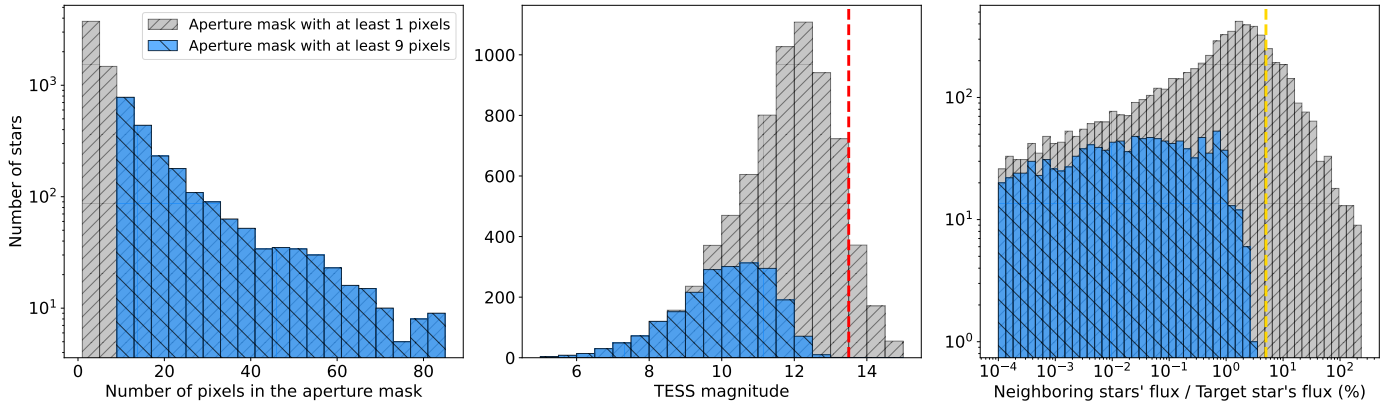

Fig. 3. Our star sample without constraints on the aperture mask size (7385 sources, grey histogram) and after imposing a minimum size of 4 pixels (2162 sources, blue histogram). Other constraints described in Section 3.1 apply to both histograms. *Left* - Sample distribution of the median aperture mask sizes, calculated per star over all TESS sectors. *Middle* - Sample distribution of the TESS magnitudes. The dashed red line marks a magnitude value of 13.5. *Right* - Median contamination level caused by neighbouring stars, calculated per star over all TESS sectors. The dashed orange line marks a contamination of 5%.

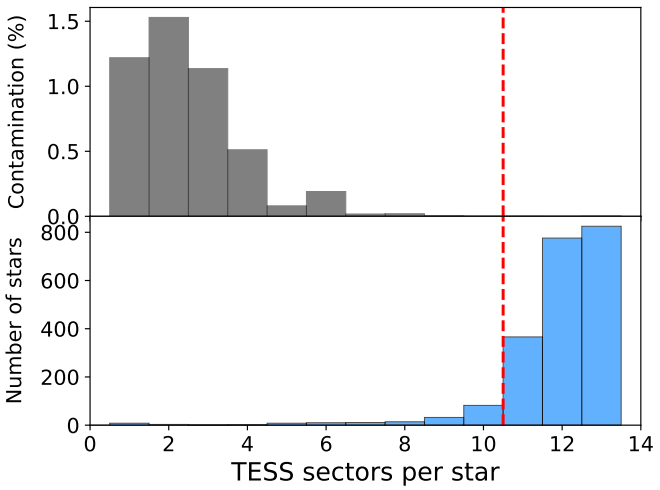

Fig. 4. The blue histogram in the bottom shows the number of TESS sectors per star with a satisfactory aperture mask. The dark-grey histogram shows the mean contamination in each bin of the blue histogram. The dashed red line shows the cut for stars with at least 11 TESS sectors (a total of 1967 stars).

and added a constant column to it to account for a constant level of background. We solved the linear regression

$$\mathbf{Y} = \mathbf{X}\mathbf{w}, \tag{4}$$

where $\mathbf{Y}$ is the uncorrected light curve of the target star and $\mathbf{w}$ are the regression coefficients. The corrected light curve was then computed as $\mathbf{Y} - \mathbf{X}\mathbf{w}$. These corrected light curves from each TESS sector were then normalised by dividing them by their mean flux. Values further away than 5σ were treated as outliers and removed (e.g. spikes due to cosmic rays). Finally, we stitched the normalised light curves as shown in Fig. 7.

4. Frequency analysis from iterative prewhitening

We analysed the light curves resulting from our developed data analysis pipeline following a procedure of iterative prewhitening. Van Beeck et al. (2021) gave an extensive description of five different prewhitening methods applied to g-mode pulsators,

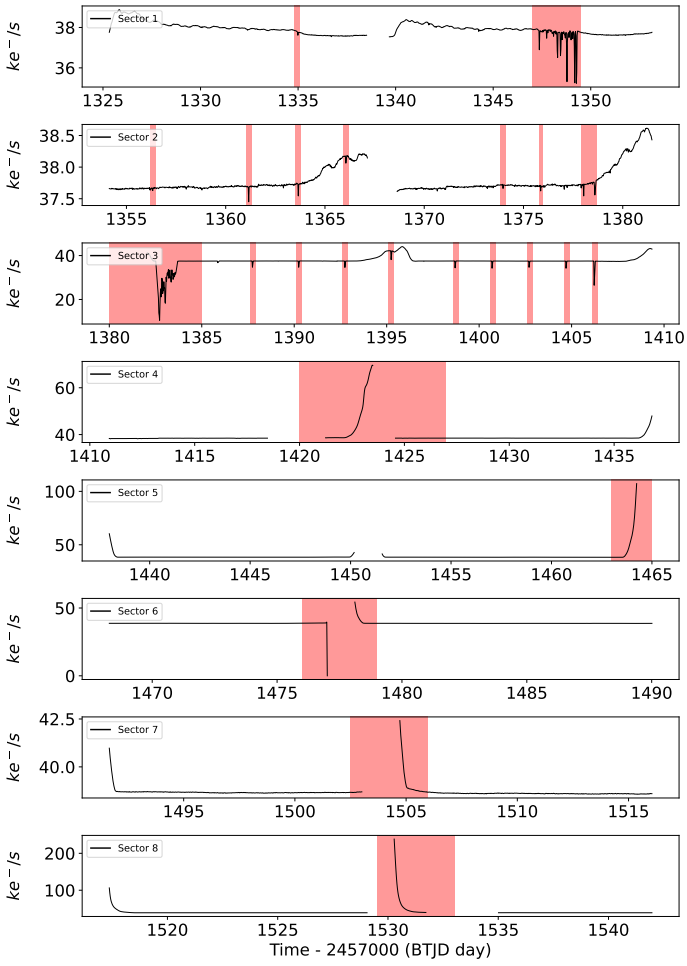

Fig. 5. Uncorrected light curves of TIC 30192406, showing in red the time intervals that have been excluded for all stars accordingly to Table A.1. Sector 1 shows an example of jittering of the satellite. Sector 2 shows an example of scattered sunlight reflected by the Earth or the Moon. Sector 3 shows an example of systematic flux variability caused by the periodic re-pointing of the camera.

relying on various regression techniques and stopping criteria. Since Van Beeck et al. (2021) developed their methodology for

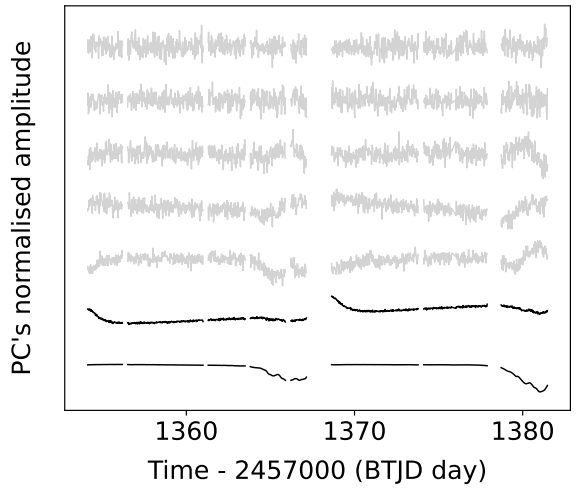

Fig. 6. The first seven PCs from the set of light curves obtained out of each background mask's pixel for the star TIC 374944608, sector 2. PCs are displayed with a shared scale and in ascending order with the first PC at the bottom. Only black PCs are used for the detrending of the light curve.

g modes in SPB stars and 4-year *Kepler* light curves, their paper is highly relevant for our TESS work as well. We avoid a detailed description here and refer to that paper for a detailed description, as well as an elaborate comparative study of the efficiency of these five methods. Here we rely on a method using the same frequency resolution restriction, a stopping criterion based on the amplitudes of the modes, and a nonlinear optimisation to achieve the final regression result, as such methods were found to be the most powerful procedures based on the assumption of a harmonic fit to the light curve by (see Van Beeck et al. 2021, Methods 2 and 3). We provide a summary of the adopted procedure, where frequencies were extracted in a 5-step process from the stitched light curves as the one shown in Fig. 7:

- **Step 1:** We computed a Lomb-Scargle periodogram of the light curve using a 10-fold oversampled frequency range (compared to T^{-1} with T the time span of the light curve) from zero up to the Nyquist frequency. The frequency with highest amplitude is selected and a harmonic fit with that frequency to the light curve is determined, using linear regression. The best-fitting harmonic function is subtracted from the light curve and the process is iteratively repeated on the residual light curve until the selected frequency has an amplitude with SNR < 4. The noise level is calculated as the mean amplitude of the periodogram within a symmetric frequency window of size 1 d^{-1} centred on the selected frequency.

  In order to find candidates with g-mode period spacing patterns, we only kept stars with at least 10 significant potential g-mode frequencies, i.e., having pulsations with periods longer than 0.25 days. This restriction, illustrated in Fig. 8, leaves us with a sample of 369 candidate stars.
- **Step 2:** Unresolved frequencies were removed by requiring a conservative difference of at least $2.5 \times T^{-1}$ between extracted frequencies (Loumos & Deeming 1978). In case of unresolved frequencies, we kept the one with the largest amplitude.
- **Step 3:** All accepted frequencies were optimised simultaneously using a Levenberg-Marquardt algorithm to perform a non-linear regression, with the output of the linear regression as initial guesses. Uncertainties in the parameters were calculated following Montgomery & O'Donoghue (1999) and corrected for their possible correlated nature following Schwarzenberg-Czerny (2003). Frequencies whose corresponding amplitudes were consistent with zero within three standard deviations were considered as insignificant and rejected.
- **Step 4:** To minimize the influence of the spectral window convolved with dominant frequencies in the periodogram during the iterative prewhitening process, we used the amplitude criterion developed by Van Reeth et al. (2015a):

$$\alpha \leq \frac{A_f}{A_{loc}} \leq \frac{1}{\alpha}\,, \tag{5}$$

  where A_f and A_{loc} are the optimised amplitudes and the amplitudes from the original Lomb-Scargle periodogram, respectively. This constraint is independent of the SNR and helps to avoid spurious frequency detections that can occur for space time-series data like TESS with SNR > 4 (e.g. Baran & Koen 2021). Moreover, Van Beeck et al. (2021) have shown criteria based on mode amplitudes to work better than just using SNR as stop criterion. In practice, we used $\alpha = 0.75$ which was found to work optimally for TESS light curves by Antoci et al. (2019).
- **Step 5:** Combination frequencies were not considered as independent mode frequencies to hunt for period spacing patterns. Such combination frequencies were identified through the following equation

$$\left| f_k - \left(n_i f_i + n_j f_j \right) \right| \leq \varepsilon\,, \tag{6}$$

  where we adopt the terminology of Degroote et al. (2009), i.e. f_i and f_j are the parent frequencies, n_i and n_j are integer combination coefficients, f_k is the combination frequency or child frequency and ε is the threshold tolerance. We selected the 20 highest-amplitude frequencies per star as parent frequencies and searched for combinations of up to two parents, i.e., $|n_i| + |n_j| \leq 2$.
  Given the large number of frequencies per star (note that Fig. 8 only counts g modes and ignores p modes), a linear combination of frequencies is likely to occur close to another frequency in the data without having to be a child frequency (Pápics 2012; Kurtz et al. 2015). This is illustrated in Fig. 9 by the background count level marked with a grey shade while genuine child frequencies correspond to the excess above such level. We therefore took three times that background level (grey dashed line in Fig. 9) as a 67% probability of being a genuine combination frequency. Such probability corresponds to $\varepsilon = 0.0002$ (red vertical line in Fig. 9) and is consistent with the threshold tolerance reported by Li et al. (2019).

Figure 10 shows the impact on the number of independent mode frequencies after each step of the frequency analysis. As an example, the final accepted frequencies of TIC 374944608 (light curve in Fig. 7) are indicated with vertical dotted lines in Fig. 16 (to be discussed below). After the frequency analysis, we checked the residual light curves and removed eclipsing binaries. These were studied further in the separate paper by IJspeert et al. (2021). We also checked cases where the light curve extraction returned over-corrected solutions. This inspection was done by eye, reducing the sample of period spacing pattern candidates to 304 stars.

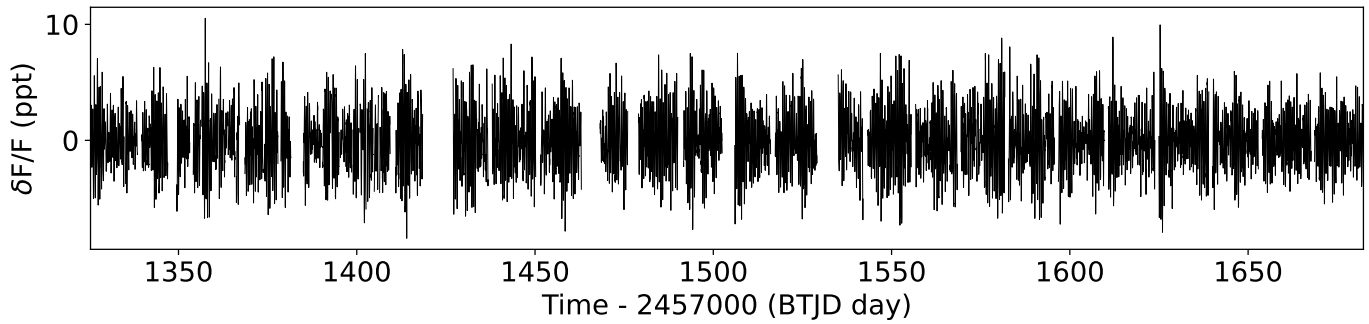

Fig. 7. Light curve for TIC 374944608 as derived from our developed pipelin discussed in Sect. 3. The flux has been divided by its median value.

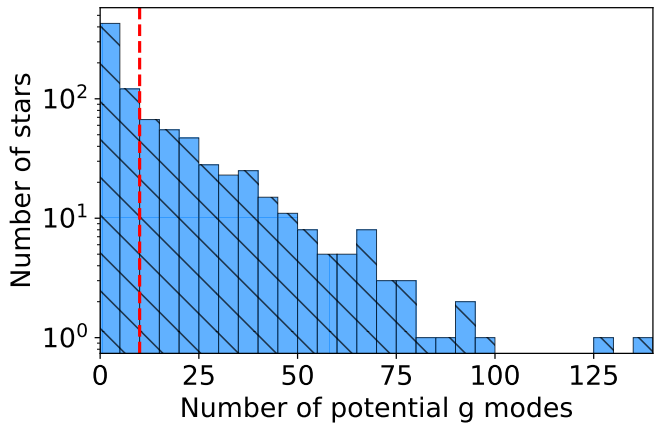

Fig. 8. Number of potential g-mode pulsations with SNR ≥ 4 per star. Frequencies were deduced from Step 1 described in Section 4. Our sample of 1967 stars has 1108 stars not complying with our Step 1 criterion and those are not plotted. The dashed red line shows the cut used to select rich enough period spacing pattern candidates, i.e. star with at least 10 significant mode periods. This resulted in 369 candidate pulsators.

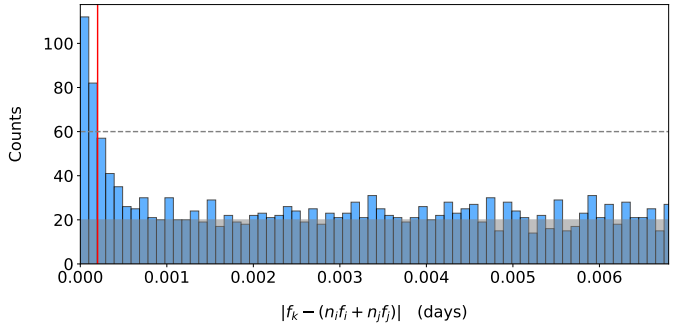

Fig. 9. Histogram following Eq. (6) for the frequencies of stars in our g-mode sample. The grey shade marks the background level that represents a random match among combination frequencies and the horizontal dashed grey line marks 3 times that level. The vertical red shows the intercept of the dashed grey line and the distribution; it marks $\varepsilon = 0.0002$ according to Eq. (6). Frequencies occurring to the left of this line have a 67% probability of corresponding to a genuine combination frequency.

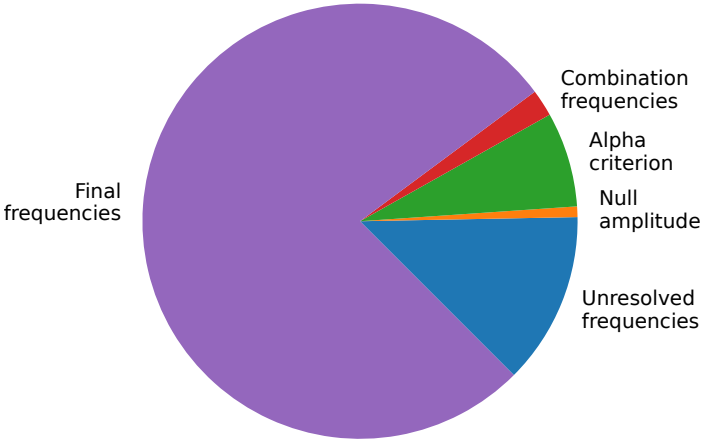

Fig. 10. Number of frequencies remaining in our sample after each step in Section 4 is applied.

5. Period-spacing pattern search

To search for period spacing patterns in our sample, we fit the following template to the list of periods of each star:

$$P_i = \sum_{j=0}^{i-1} \Delta P_j + P_0 = \Delta P_0 \frac{(1+\Sigma)^i - 1}{\Sigma} + P_0 \tag{7}$$

where $\Delta P_j = P_{j+1} - P_j$ is the local period spacing and ΔP_0 is the period spacing at a reference period P_0. This period pattern allows for a linear change $\Sigma \equiv \mathrm{d}(\Delta P)/\mathrm{d}P$ of the local period spacing caused by stellar rotation (Ouazzani et al. 2017; Li et al. 2019). The template depends on the three parameters $\{P_0, \Delta P_0, \Sigma\}$. To fit Eq. (7) to the observations, we minimised the following custom cost function:

$$S\,(P_0, \Delta P_0, \Sigma) = \sum_{i=1}^{n} \frac{A_i}{A_{\max}} \frac{\left(P_i^{\mathrm{obs}} - P_i\right)^2}{\sigma_i^2 + \Delta P_i^2}\ , \tag{8}$$

where P_i is the estimated period closest to the observed pulsation period P_i^{obs}, ΔP_i is the estimated local period spacing, A_i is the observed amplitude corresponding to P_i^{obs}, and $A_{\max}$ is the maximum observed amplitude. Rather than minimising the (square of the) absolute differences $(P_i^{\mathrm{obs}} - P_i)^2$ we minimise the relative differences $(P_i^{\mathrm{obs}} - P_i)^2/\Delta P_i^2$. In this way, period mismatches are more strongly penalised when they are large compared to the local period spacing. The addition of the observed period uncertainty σ_i^2 serves to limit this stronger penalisation when the local period spacing is comparable to the observational period uncertainty σ_i. The extra weight $A_i/A_{\max}$ serves to penalise a pattern

more strongly when it mismatches the higher amplitude mode periods. The minimisation of the cost function S was done with the quasi-Newton method L-BFGS-B (Byrd et al. 1995) implemented in the Python module `Scipy` (Virtanen et al. 2020).

To find the location of the patterns in the periodogram as well as the initial guesses $\theta^{\rm init} = \{P_0^{\rm init}, \Delta P_0^{\rm init}, \Sigma^{\rm init}\}$ for the fit, we used two diagnostic plots to cover both the cases of rapid and slow rotators. Slow rotators show an approximately constant period spacing. Their period spacing pattern can therefore be identified in an échelle diagram, where the period is plotted as a function of the period modulo ΔP. In such a case, g modes of a given angular degree roughly form vertical ridges (analogous to the acoustic modes in the case of solar-like oscillations). On the other hand, rapid rotators show a period spacing that depends approximately linearly on the mode period (Van Reeth et al. 2016; Ouazzani et al. 2017). Therefore their period spacing pattern can be easier identified in a plot of ΔP as a function of period. For each star, we also complemented such two plots with a periodogram where observed and template periods were overplotted.

To facilitate the exploration of the parameter space, we developed the interactive tool `FLOSSY`[6]. `FLOSSY` is a Python utility that allows to efficiently browse the periodogram of a large number of stars and visualise the period spacing patterns by displaying the period échelle diagram and period spacing plot at each location in the periodogram. `FLOSSY` also overplots Eq. (7) in the aforementioned plots with customised parameters $\{P_0, \Delta P_0, \Sigma\}$. The latter can be modified on the fly along with the number of mode periods to fit. Figure 16 shows part of `FLOSSY`'s output, as well as the best-fit pattern for TIC 374944608.

We used `FLOSSY` to manually select the $\theta^{\rm init}$ for every candidate period spacing pattern found from the list of mode periods per star. In doing so we considered the parameter space $|P_0 - P_0^{\rm init}| \leq \delta P/2$, 100 s $\leq \Delta P_0 \leq$ 4000 s and, $-0.3 \leq \Sigma \leq 0.3$, where $P_0^{\rm init} \in \{P_i^{\rm obs}\}$ and δP corresponds to the resolution set in **Step 2** of the procedure discussed in Section 4. To ensure that we found a global minimum, we computed S around the best-fit solution in a radius of 400 s for P_0, 40 s for ΔP_0, and 0.05 units for Σ. Those values for S are shown in Fig. 17, which is also an output of `FLOSSY`.

To estimate uncertainties for the detected period spacing pattern, we computed the 95% confidence interval of the parameters using a bootstrap method with non-parametric resampling in the periodogram. We generated 10000 datasets of the same size as the original one, with replacement. Subsequently we minimised Eq. 8 in each of these datasets using as initial guess the same $\theta^{\rm init}$ as in the original best fit. The confidence intervals were then determined as the 2.5% and 97.5% quantiles of the bootstrap distribution for the parameters θ. As an example, Fig. 11 shows the bootstrap distribution of Σ for the pattern found in TIC 374944608.

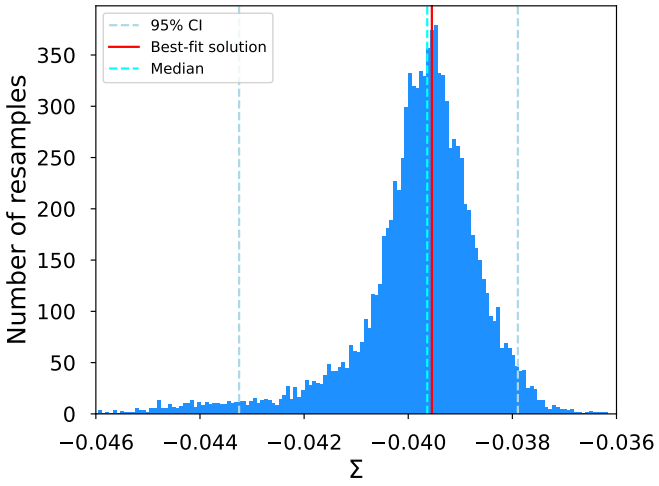

Fig. 11. Confidence interval for Σ according to Eq. (7) following a bootstrap procedure for TIC 374944608. The meaning of the various vertical dashed lines are indicated in the legend.

6. Catalogue of g-mode pulsators in the TESS S-CVZ with identified period spacing patterns

Our final catalogue of g-mode pulsators revealing period spacing patterns consists of 130 bright dwarfs in the TESS S-CVZ. These stars revealed a total of 174 resolved period spacing patterns as listed in Table A.2. Each of those is provided in Appendix A in the same format as Figs 16 and 17. The stars in our catalogue have apparent TESS magnitudes within the range 7 to 12, with a median of ~ 9.8. TIC 350144657 is an exception to this with an apparent TESS magnitude of ~ 5.1.

The level of contamination of individual light curves (due to neighbouring stars) is < 2% as a result of our stringent requirements on the aperture mask as described in Section 3.1. Figure 12 shows the distributions in terms of brightness and contamination for all the pulsators in the catalogue. Only two stars in our catalogue, TIC 300746044 and TIC 375038081, are candidate SPB stars as determined by the colour-magnitude selection done in Section 2, while the other members of the catalogue are γ Dor stars. Figure 13 shows a *Gaia* CMD comparing our catalogue to the 611 γ Dor stars with detected period spacing patterns found by Li et al. (2020) in 4-year *Kepler* light curves. We find that our catalogue stars occur on the hotter end of the *Kepler* γ Dor stars.

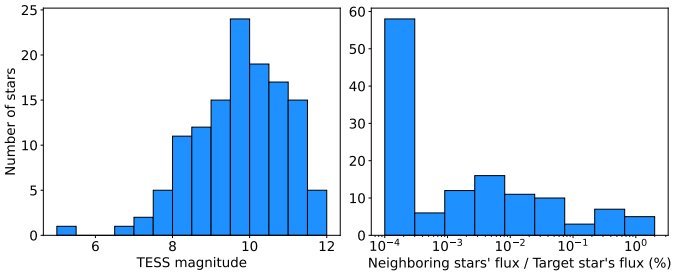

Fig. 12. Magnitude (left, apparent TESS magnitude) and median contamination level in the aperture mask caused by flux of neighbouring stars, calculated over all TESS sectors (right) distributions of stars in the catalogue.

Out of the 174 period spacing patterns, there are 108 with a downward slope ($\Sigma < 0$) and 66 with an upward slope ($\Sigma > 0$). The former are prograde or zonal g modes while the latter are retrograde g modes or Rossby modes (Van Reeth et al. 2016). The smallest averaged period spacing value per pattern, $\langle \Delta P \rangle$, is ~ 133 s. The shortest pattern contains 4 measured pulsation periods, while more than half of the patterns contain more than 12 detected pulsation periods. The longest pattern contains 18 measured pulsation periods.

In 29% of the stars we detected two or three patterns. When multiple patterns are detected for an individual star, this allows

[6] `https://github.com/IvS-KULeuven/FLOSSY`

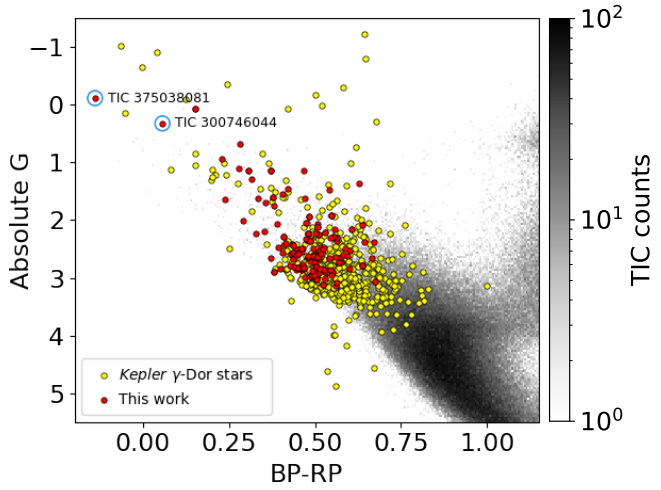

Fig. 13. *Gaia* CMD showing our sample (red) and the 611 γ-Dor stars with period-spacing patterns found by Li et al. (2020) in *Kepler* data (yellow). Stars marked with blue circles are SPB candidates. Background stars correspond to the TESS S-CVZ. Magnitudes are not corrected for extinction

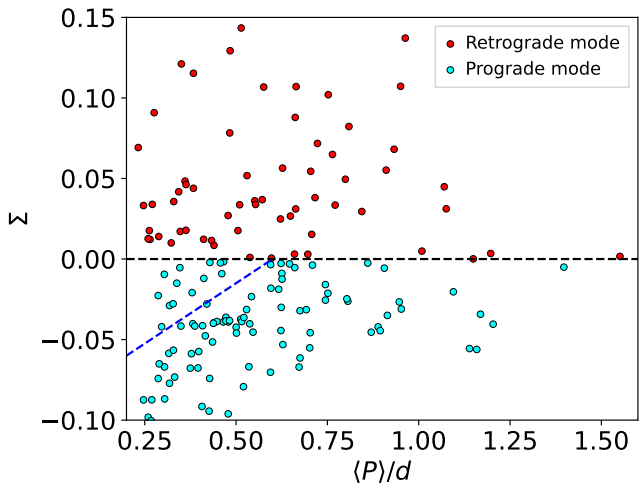

Fig. 14. The P-Σ relation for g-mode pulsators in our catalogue. The dashed blue line is the empirical cut from Li et al. (2020) that separates prograde $\ell = 1$ g modes (below) from $\ell = 2$ (above).

for better constraints of the stellar interior from asteroseismic modelling (Aerts et al. 2018). Furthermore, 33% of our catalogue stars are hybrid pulsators, i.e., they also exhibit p-mode pulsations, which provide a mean to probe the outer stellar envelope allowing for a differential study.

Figure 15 shows the distributions of the pattern parameters. The pattern slopes fulfill $|\Sigma| \leq 0.1$ for 86% of the catalogue stars, while the tails of the distribution reach $|\Sigma| \sim 0.2$. Using the empirical relations in Li et al. (2020), we estimate the near-core rotation to be $< 1.68\,\mathrm{d}^{-1}$ for 86% of the stars in our sample, with a few stars reaching up to $\sim 2.86\,\mathrm{d}^{-1}$. We also made use of the empirical cut delineating regimes of dipole and quadrupole modes introduced by Li et al. (2020) in Fig. 14 (dashed blue line). This suggests that 13 of our catalogue stars with $\Sigma < 0$ have $\ell = 2$ modes while the other pulsators have $\ell = 1$. Because pulsations in γ Dor stars are sensitive to metallicity, the estimates above remain to be confirmed. Since the nominal *Kepler* field-of-view was in the Northern Hemisphere, we cannot cross-validate our TESS S-CVZ results with those from *Kepler*.

Furthermore, we note that the range in overtones in the patterns is a proxy for the radial order n of the g modes. The exact value of n, ℓ and m can only be identified from asteroseismic modelling, e.g. based on the traditional approximation of rotation (TAR Eckart 1960) as applied in Van Reeth et al. (2016). The mode identifcation and asteroseismic modelling based on it will be addressed in a future paper dedicated to the ensemble of stars in our catalogue of g-mode pulsators, relying on the pattern properties deduced in this work.

Besides quasi-linear period spacing patterns like the one shown in panel Ⓒ of Fig. 16, where the zigzag feature is caused by missing periods in the pattern, our catalogue contains tens of patterns with zigzag signatures that are not related to missing modes. This is discussed in the online Appendix B. Such signatures have also been observed in period spacing patterns of SPB stars, where they are interpreted as a result of strong envelope mixing deep inside the star. These signatures were recently used by Pedersen et al. (2021) to constrain the internal mixing profile in SPB stars observed by *Kepler*. The levels of envelope mixing found thus far in γ Dor stars are far lower than those of SPB stars (cf. Table 1 in Aerts 2021). Our catalogue presents an opportunity to further assess and refine these recent conclusions in the literature from our TESS S-CVZ catalogue of g-mode dwarf pulsators.

Finally, we noted that 14 of the detected period spacing patterns in our catalogue show residuals with a clear modulated sinusoidal shape, like the one shown in panel Ⓑ of Fig. 16. This type of periodic residuals is very similar to the one found originally for the slowly-rotating CoRoT SPB HD 50230 by Degroote et al. (2010) and allows for stringent constraints on the core overshooting and envelope mixing.

7. Conclusion

In this work, we presented a new data analysis pipeline to create light curves from TESS FFIs, with emphasis on the search for g-mode frequencies in intermediate- to high-mass stars. We presented guidelines for extracting light curves from unprocessed TESS images, including the selection of aperture and background masks, the identification of time stamps affected by systematics in sectors 1-13 of the TESS S-CVZ, and a modified principal component analysis to detrend the light curves. A colour-magnitude criterion was presented as a fast method to identify main-sequence A/F- and O/B-type star candidates.

Based on the light curves extracted with our pipeline, we composed the first catalogue of g-mode period spacing patterns detected in TESS space photometry of dwarfs having colours representative of spectral types F to O. Our catalogue contains 174 g-mode period spacing patterns observed in 128 γ Dor stars and 2 SPB stars. The patterns were manually reviewed and contain g-mode frequencies having amplitudes with SNR>4. In future work, we will use the detected patterns to derive the internal rotation frequency near the convective core of the stars, as well as the buoyancy travel time across the stars (known as Π_0). These two key quantities constitute important observables to perform asteroseismic modelling of intermediate-mass stars (e.g., Mombarg et al. 2021; Pedersen et al. 2021). We also introduced `FLOSSY`, an open source utility to inspect periodograms of g-mode pulsators to facilitate searches for period spacing patterns.

The nominal frequency resolution of modes in the detected patterns amounts to $0.003\mathrm{d}^{-1}$, following the 352 d long TESS S-CVZ light curves. This frequency resolution can be improved

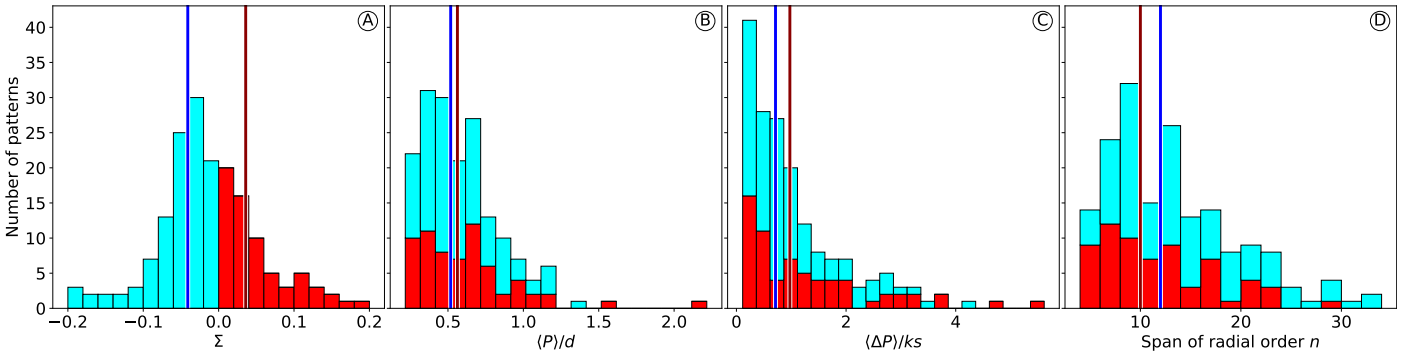

Fig. 15. Characterisation of the best-fit patterns in our sample (see also Table A.2). The stacked histograms show retrograde modes in red and prograde modes in cyan. The vertical brown and blue lines are the median of the retrograde and prograde distributions, respectively. Ⓐ **:** Slope $\Sigma \equiv \mathrm{d}\Delta P/\mathrm{d}P$. Ⓑ **:** Mean period $\langle P \rangle$. Ⓒ **:** Mean period spacing $\langle \Delta P \rangle$. Ⓒ **:** Number of overtones.

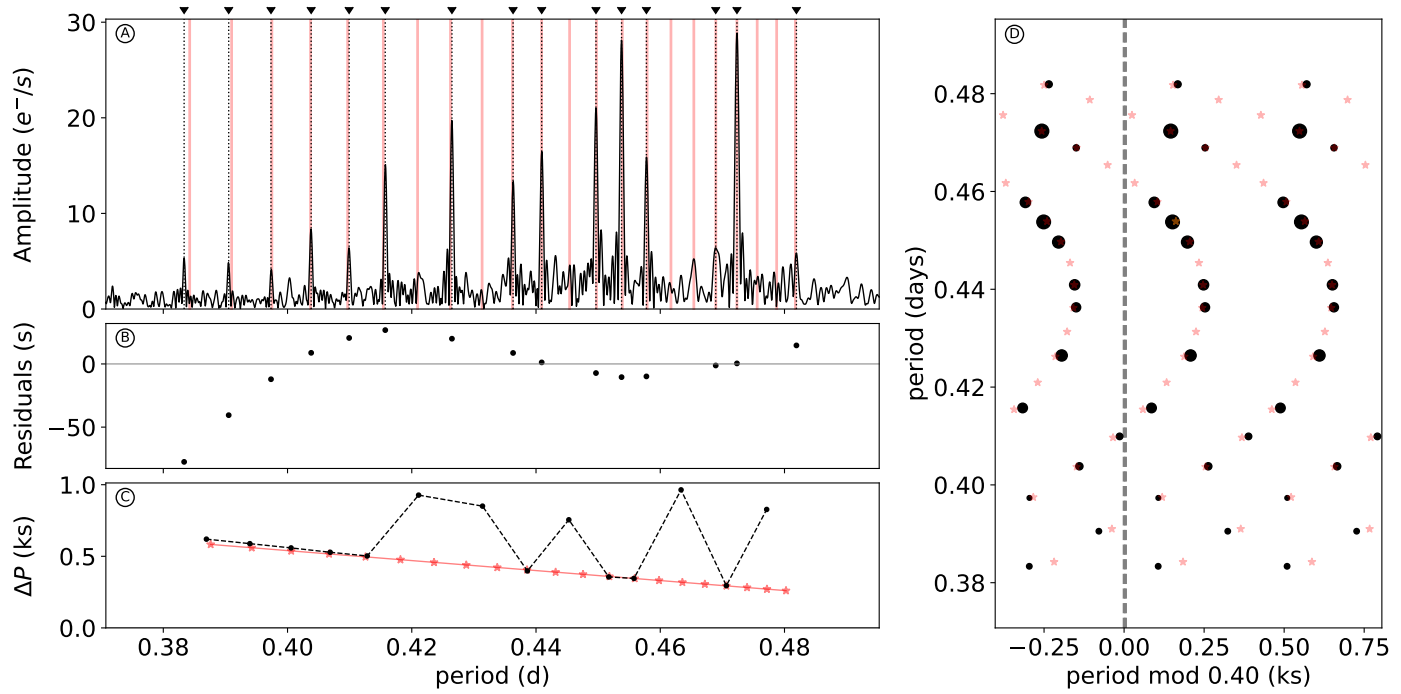

Fig. 16. Best-fit period spacing pattern for TIC 374944608. Plots generated with the interactive code `FLOSSY`. Ⓐ **:** LS periodogram (solid black line), observed periods (vertical dotted black lines), best-fit linear template (vertical red lines). Observed periods that are consistent with the best-fit linear pattern within a quarter of the local ΔP are indicated by black triangles. Ⓑ **:** Deviations from the linear pattern (i.e., difference between the periods indicated by the black triangles and the red vertical lines). Ⓒ **:** Period spacing as a function of mode period. The black dots connected by the dashed line segments are the observations and the red solid line is the best-fit linear pattern with slope Σ. Note that missing mode periods in the observations create artificially larger ΔP values. Ⓓ **:** échelle diagram.

by a factor 3 when the extended TESS Cycle 3 data will be included in the analysis. This will also lower the noise level in the Fourier domain and offers the future potential to detect more modes per star, as well as more stars with g-mode patterns. The global properties of the detected patterns occurring in our catalogue are listed in Table A.2 and the patterns themselves are shown in Appendix A. This catalogue constitutes a base for future ensemble asteroseismic modelling of TESS g-mode pulsators following methodologies as in Mombarg et al. (2021) or Pedersen et al. (2021). In this way, we will be able to constrain the internal physics of more rotating dwarfs with a convective core using the new available TESS data, in addition to the asteroseismic modelling achieved so far for a legacy sample of g-mode pulsators from the *Kepler* mission (Gebruers et al. 2021). This will increase the number of dwarfs with such modelling and will lead to a better understanding of the transport processes and their relationship to the internal rotation profile of these stars.

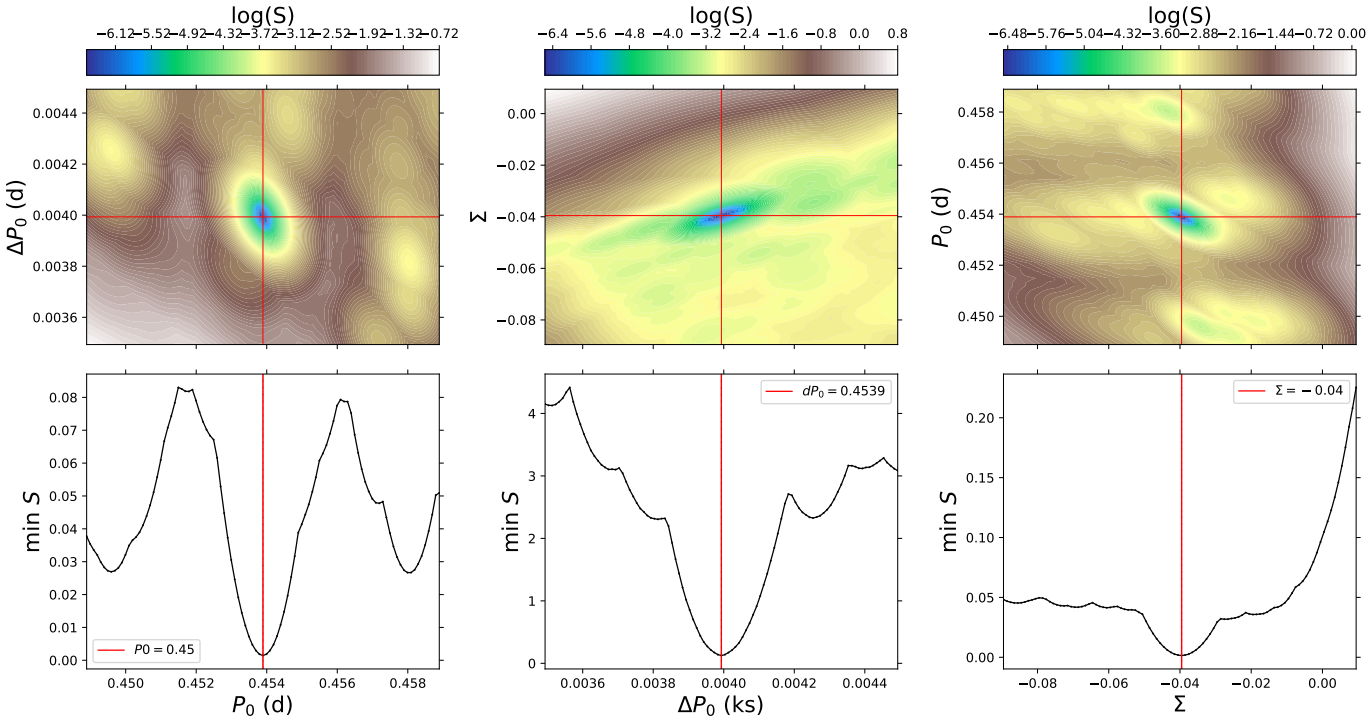

Fig. 17. Uncertainty estimates of results for TIC 374944608 shown in Fig. 16. Plots generated with the interactive code `FLOSSY`. **Top -** Correlation plots. **Bottom -** Minimum value of the cost function S as a function of the template period spacing parameters.

Appendix A: Appendix 1

Table A.1. Intervals excluded from the light curves to removed sytematics such as scattered light, telescope jittering and loss of fine pointing.

TESS sector	Excluded interval [days]
1	(1334.8, 1335.1)
	(1347.0, 1349.5)
2	(1356.2, 1356.5)
	(1361.0, 1361.3)
	(1363.5, 1363.8)
	(1365.9, 1366.2)
	(1373.8, 1374.1)
	(1375.8, 1376.0),
	(1377.9, 1378.7)
3	(1380.0, 1385.0)
	(1387.6, 1387.9)
	(1390.1, 1390.4)
	(1392.6, 1392.9)
	(1395.1, 1395.4)
	(1398.6, 1398.9)
	(1400.6, 1400.9)
	(1402.6, 1402.9)
	(1404.6, 1404.9)
	(1406.1, 1406.4)
4	(1420.0, 1427.0)
5	(1463.0, 1465.0)
6	(1476.0, 1479.0)
7	(1502.5, 1506.0)
8	(1529.5, 1533.0)

Acknowledgements. The research leading to these results has received funding from the European Research Council (ERC) under the European Union's Horizon 2020 research and innovation programme (grant agreement no. 670519: MAMSIE) and from the KU Leuven Research Council (grant C16/18/005: PARADISE). TVR gratefully acknowledges support from the Research Foundaton Flanders under grant agreement nr. 12ZB620N. In addition to the software cited in the main body of the paper we have also made use of Lightkurve, a Python package for *Kepler* and TESS data analysis (Lightkurve Collaboration et al. 2018), Astropy,[7] a community-developed core Python package for Astronomy (Astropy Collaboration et al. 2013, 2018), Matplotlib (Hunter 2007), NumPy (Harris et al. 2020), SciPy (Virtanen et al. 2020), pandas (Wes McKinney 2010)

References

Aerts, C. 2021, Reviews of Modern Physics, 93, 015001
Aerts, C., Christensen-Dalsgaard, J., & Kurtz, D. W. 2010, Asteroseismology, Springer-Verlag, Heidelberg
Aerts, C., Mathis, S., & Rogers, T. M. 2019, ARA&A, 57, 35
Aerts, C., Molenberghs, G., Michielsen, M., et al. 2018, The Astrophysical Journal Supplement Series, 237, 15
Aerts, C., Van Reeth, T., & Tkachenko, A. 2017, ApJ, 847, L7
Antoci, V., Cunha, M. S., Bowman, D. M., et al. 2019, MNRAS, 490, 4040
Arenou, F., Luri, X., Babusiaux, C., et al. 2018, A&A, 616, A17
Astropy Collaboration, Price-Whelan, A. M., Sipőcz, B. M., et al. 2018, AJ, 156, 123
Astropy Collaboration, Robitaille, T. P., Tollerud, E. J., et al. 2013, A&A, 558, A33
Auvergne, M., Bodin, P., Boisnard, L., et al. 2009, A&A, 506, 411
Bailer-Jones, C. A. L., Rybizki, J., Fouesneau, M., Mantelet, G., & Andrae, R. 2018, AJ, 156, 58
Baran, A. S. & Koen, C. 2021, A Detection Threshold in the Amplitude Spectra Calculated from TESS Time-Series Data
Bouabid, M. P., Dupret, M. A., Salmon, S., et al. 2013, MNRAS, 429, 2500
Brasseur, C. E., Phillip, C., Fleming, S. W., Mullally, S. E., & White, R. L. 2019, Astrocut: Tools for creating cutouts of TESS images
Byrd, R. H., Lu, P., Nocedal, J., & Zhu, C. 1995, SIAM Journal on Scientific Computing, 16, 1190
Caldwell, D. A., Tenenbaum, P., Twicken, J. D., et al. 2020, Research Notes of the AAS, 4, 201
Christophe, S., Ballot, J., Ouazzani, R. M., Antoci, V., & Salmon, S. J. A. J. 2018, A&A, 618, A47
Cunha, M. S., Avelino, P. P., Christensen-Dalsgaard, J., et al. 2019, MNRAS, 490, 909
Degroote, P., Aerts, C., Baglin, A., et al. 2010, Nature, 464, 259
Degroote, P., Briquet, M., Catala, C., et al. 2009, A&A, 506, 111
Eckart, C. 1960, Physics of Fluids, 3, 421
García, R. A. & Ballot, J. 2019, Living Reviews in Solar Physics, 16, 4
Gebruers, S., Straumit, I., Tkachenko, A., et al. 2021, A&A, 650, A151
Handberg, R., Lund, M., & Huber, D. 2019, TESS Data For Asteroseismology Lightcurves ("TASOC")
Harris, C. R., Millman, K. J., van der Walt, S. J., et al. 2020, Nature, 585, 357
Hekker, S. & Christensen-Dalsgaard, J. 2017, The Astronomy and Astrophysics Review, 25
Huang, C. X. 2020, TESS Lightcurves From The MIT Quick-Look Pipeline ("QLP")
Hunter, J. D. 2007, Computing in Science & Engineering, 9, 90
IJspeert, L. W., Tkachenko, A., Johnston, C., et al. 2021, A&A, in press, arXiv:2107.10005
Kaye, A. B., Handler, G., Krisciunas, K., Poretti, E., & Zerbi, F. M. 1999, PASP, 111, 840
Kippenhahn, R., Weigert, A., & Weiss, A. 2012, Stellar Structure and Evolution
Koch, D. G., Borucki, W. J., Basri, G., et al. 2010, ApJ, 713, L79
Kurtz, D. W., Shibahashi, H., Murphy, S. J., Bedding, T. R., & Bowman, D. M. 2015, MNRAS, 450, 3015
Lee, U. 2021, MNRAS, 505, 1495
Li, G., Bedding, T. R., Murphy, S. J., et al. 2019, MNRAS, 482, 1757
Li, G., Van Reeth, T., Bedding, T. R., et al. 2020, MNRAS, 491, 3586
Lightkurve Collaboration, Cardoso, J. V. d. M., Hedges, C., et al. 2018, Lightkurve: Kepler and TESS time series analysis in Python, Astrophysics Source Code Library
Loumos, G. L. & Deeming, T. J. 1978, Ap&SS, 56, 285
Miglio, A., Montalbán, J., Noels, A., & Eggenberger, P. 2008, MNRAS, 386, 1487
Mombarg, J. S. G., Dotter, A., Van Reeth, T., et al. 2020, ApJ, 895, 51
Mombarg, J. S. G., Van Reeth, T., & Aerts, C. 2021, A&A, 650, A58
Mombarg, J. S. G., Van Reeth, T., Pedersen, M. G., et al. 2019, MNRAS, 485, 3248
Montgomery, M. H. & O'Donoghue, D. 1999, Delta Scuti Star Newsletter, 13, 28
Ouazzani, R. M., Lignières, F., Dupret, M. A., et al. 2020, A&A, 640, A49
Ouazzani, R.-M., Salmon, S. J. A. J., Antoci, V., et al. 2017, MNRAS, 465, 2294
Pápics, P. I. 2012, Astronomische Nachrichten, 333, 1053
Pápics, P. I., Tkachenko, A., Van Reeth, T., et al. 2017, A&A, 598, A74
Pedersen, M. G., Aerts, C., Pápics, P. I., et al. 2021, Nature Astronomy
Pedersen, M. G., Chowdhury, S., Johnston, C., et al. 2019, The Astrophysical Journal Letters, 872, l9
Ricker, G. R., Winn, J. N., Vanderspek, R., et al. 2015, Journal of Astronomical Telescopes, Instruments, and Systems, 1, 014003
Ruppert, D. 2011, Statistics and Data Analysis for Financial Engineering (Springer New York)
Saio, H., Takata, M., Lee, U., Li, G., & Van Reeth, T. 2021, MNRAS, 502, 5856
Schmid, V. S. & Aerts, C. 2016, A&A, 592, A116
Schwarzenberg-Czerny, A. 2003, in Astronomical Society of the Pacific Conference Series, Vol. 292, Interplay of Periodic, Cyclic and Stochastic Variability in Selected Areas of the H-R Diagram, ed. C. Sterken, 383
Shibahashi, H. 1979, PASJ, 31, 87
Stassun, K. G., Oelkers, R. J., Paegert, M., et al. 2019, The Astronomical Journal, 158, 138
Szewczuk, W., Walczak, P., & Daszyńska-Daszkiewicz, J. 2021, MNRAS, 503, 5894
Takata, M., Ouazzani, R. M., Saio, H., et al. 2020, A&A, 635, A106
Tassoul, M. 1980, ApJS, 43, 469
Tkachenko, A., Aerts, C., Yakushechkin, A., et al. 2013, A&A, 556, A52
Townsend, R. H. D., Goldstein, J., & Zweibel, E. G. 2018, MNRAS, 475, 879
Townsend, R. H. D. & Teitler, S. A. 2013, MNRAS, 435, 3406
Twicken, J. D., Caldwell, D. A., Jenkins, J. M., et al. 2020, TESS Science Data Products Description Document: EXP-TESS-ARC-ICD-0014 Rev F, Tech. Rep. 20205008729, NASA
Van Beeck, J., Bowman, D. M., Pedersen, M. G., & et al. 2021, A&A, under revision
Van Beeck, J., Prat, V., Van Reeth, T., et al. 2020, A&A, 638, A149
Van Reeth, T., Mombarg, J. S. G., Mathis, S., et al. 2018, A&A, 618, A24
Van Reeth, T., Tkachenko, A., & Aerts, C. 2016, A&A, 593, A120
Van Reeth, T., Tkachenko, A., Aerts, C., et al. 2015a, A&A, 574, A17
Van Reeth, T., Tkachenko, A., Aerts, C., et al. 2015b, ApJS, 218, 27
Virtanen, P., Gommers, R., Oliphant, T. E., et al. 2020, Nature Methods, 17, 261
Waelkens, C. 1991, A&A, 246, 453
Wes McKinney. 2010, in Proceedings of the 9th Python in Science Conference, ed. Stéfan van der Walt & Jarrod Millman, 56 – 61
Wu, T. & Li, Y. 2019, ApJ, 881, 86

[7] http://www.astropy.org